Geophysical Research Letters®

Key Points:
- Yan'an new urban area subsides at 70 mm/year, in proportion to the amount of the filling mass
- Decelerating settlement is expected to reach stabilization by 2030
- Elastic stress changes amount to hundreds of kPa in the shallow zone of anthropogenic loading and unloading

Remote Sensing Characterization of Mountain Excavation and City Construction in Loess Plateau

Xie Hu[1] ⬝, **Liang Xue[2]** ⬝, **Yongtang Yu[3]**, **Songfeng Guo[4]** ⬝, **Yifei Cui[5]** ⬝, **Yao Li[6]** ⬝, and **Shengwen Qi[4]** ⬝

[1]College of Urban and Environmental Sciences, Peking University, Beijing, China, [2]Department of Earth and Environmental Sciences, Syracuse University, Syracuse, NY, USA, [3]China Jikan Research Institute of Engineering Investigations and Design, Co., Ltd., Xi'an, China, [4]Key Laboratory of Shale Gas and Geoengineering, Institute of Geology and Geophysics, Chinese Academy of Sciences, Beijing, China, [5]Department of Hydraulic Engineering, Tsinghua University, Beijing, China, [6]Institute of Mountain Hazards and Environment, Chinese Academy of Sciences, Chengdu, China
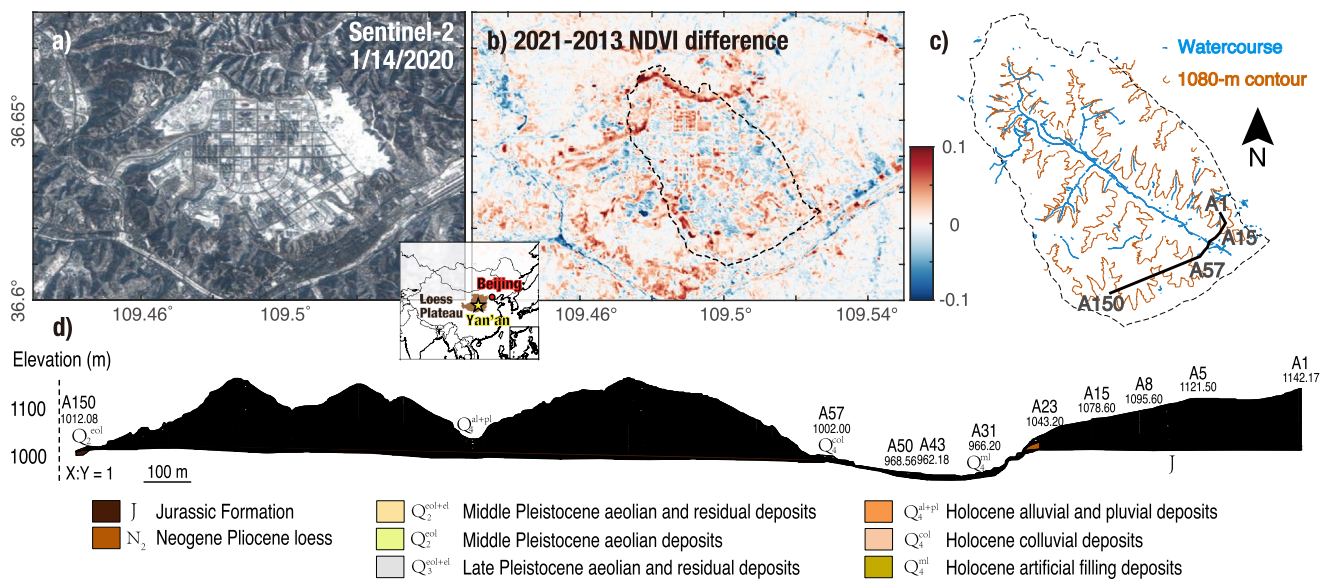
Abstract The demand for land exploitation to accommodate increasing population in metropolis is escalating worldwide. The unprecedented Mountain Excavation and City Construction project in the hilly gully Loess Plateau of China is a crustal surgery to seek the balance between urbanization and sustainability in the forerunner Yan'an city. Here, we rely on multisource remote sensing imagery to characterize the contemporary anthropogenic modification of the loess landscape. The topography has been reshaped with ±80-m elevation changes and 1.28×10^8-m^3 mass transfer by 2015. The subsidence rates at up to ~70 mm/year during 2014–2020 are proportional to the amount of the filling mass, which is expected to reach stabilization by 2030. Hundreds-of-kilopascal stress changes are distributed in the shallow zone due to the mass transfer. Continuous monitoring is an integral part of hazard mitigation in this naturally landslide hazard-prone loess environment.

Plain Language Summary The land usage has become a global crisis with increasing population and diminishing habitats in the context of climate change. How can we human beings modify the harsh environment for urbanization? Unprecedented crustal surgery in the forms of hilltop cuts and gully fills is happening over the Loess Plateau of China. Tens of square kilometers of new land flattened in Yan'an. We use multisource remote sensing imagery to quantify the spatiotemporal surface changes and ground deformation, to predict the length of time it needs to be stabilized, and to model the consequent stress changes in the hazard-prone loess landscapes. This study demonstrates the full potentials of remote sensing in characterizing the human-nature interactions.

1. Introduction

The population growth and urban expansion aggravate the tension between human and ecological environment, especially for the naturally fragile environments. The Loess Plateau in the vast mid-north China, including Shaanxi, Gansu, and Sichuan Provinces, covers an area of 624,641 km² (Wang, 2017). The loess is composed of million-year-old thick deposits of windblown dust and silt, which are subject to disaggregation under harsh climatic and soil conditions. The natural and anthropogenic deforestation has accelerated the erosion, leading to various geological hazards such as droughts and floods, monsoonal summertime landslides, and springtime sandstorms.

Although the early civilizations heavily relied on agriculture benefiting from fertile soils, the intensive soil erosion and channel incision have transformed 70% of the original flat plateau into the hilly gully landscape over thousands of years (Fu et al., 2017). Local farmers were in poverty as their efforts can hardly be paid off due to inappropriate soil conditions and multihazard scenarios. To mitigate soil erosion and desertification, as well as to restore the forest landscape for a sustainable development in northern China, the government dedicated to the Grain for Green Program (a.k.a., Conversion of Cropland to Forest Program) during 1999–2008, along with several nationwide campaigns launched in late 1990s, such as the Natural Forest Protection Program and the Sloping Land Conversion Program (Feng et al., 2016; Fu et al., 2017). About 15 million hectares of farmland and 17 million hectares of barren or degraded mountainous wasteland have

Figure 1. Map of the new urban area in Yan'an, China. (a) Optical image obtained in 2020 by Sentinel-2 satellite (See Figure S1 for historic optical images). (b) Differential Normalized Difference Vegetation Index (NDVI) between March 27, 2021 and April 3, 2013 derived from Landsat-8 satellite. Positive values mean increasing vegetation index. (c) Elevation contours and watercourse. (d) Geological cross section along the black line in panel (c).

been reversed to natural vegetation. The Grain for Green project successfully increases the Normalized Difference Vegetation Index (NDVI) by 0.023 in Yan'an, the capital city of Shaanxi Province (He et al., 2020). Nonetheless, the nature-human tension was not evidently alleviated due to urban growth. In response to the Chinese Western Development Policy and the Belt and Road Policy, the government proposed the Mountain Excavation and City Construction (MECC) project (a.k.a., Gully Land Consolidation project) in December 2011 (e.g., Juang et al., 2019; Liu et al., 2017).

Artificial modification of the mountainous landscape is not new. Mountaintop removal was implemented in eastern United States in late 20th century for the low sulfur, high-grade coal mining (Burns, 2007; Crotty, 2002). Here, Yan'an was chosen as a testbed and forerunner of MECC due to its comparatively gentle topographic gradients. The 36-km^2 original urban area of Yan'an is the home to approximately 500k people. The population density (~14,700 per km^2) is comparable to the metropolis Beijing and Shanghai. Some parts of Yan'an are far below the national standard of the area per capita. The mega-engineering MECC project started in April 2012 (Figure S1). About 78.5-km^2 new urban areas are expected by the end of this project (Li et al., 2014). This major surgery on the hilly topography started from 10.5-km^2 landscape with excavations by 200 million m^3 and fills by 163 million m^3. A total of 33 hilltops have been cut and dozens of gullies have been filled to create the flat terrain. The topographic relief of the affected areas is as large as 308 m. The dramatic changes of the landform and landscape perturb watercourses in recharge, discharge, groundwater preserved in vegetation, orographic precipitation, wind direction, sediment flux, and channel and hillslope behaviors on different spatiotemporal scales (Figure 1). Such anthropogenic mass redistributions inevitably break the subsurface stress equilibrium. Beyond that, loess materials are naturally subject to irregular wetting-induced compaction, which may lead to cracks on the roads, infrastructures, pipelines, and even catastrophic collapses.

SAR remote sensing has manifested its versatility in characterizing the ground deformation in various landscapes at different spatiotemporal scales such as on critical infrastructures, coastal and inland urban regions, archeological sites, landslides, permafrost, glaciers, earthquakes, and volcanoes (e.g., Biggs & Wright, 2020; Chen, Guo, et al., 2017; Chen, Wu, et al., 2017; Handwerger et al., 2019; Li, Li, et al., 2018; Lu & Dzurisin, 2014; Schaefer et al., 2019; Shirzaei et al., 2020; Xu et al., 2020). InSAR studies over Yan'an is not new (e.g., Wu et al., 2019; Zhang, Zhu, et al., 2020; Xu et al., 2021); however, the attendant ground deformation and subsurface stress distribution have not been quantitatively investigated and verified.

Here, we first introduce the geological and hazardous environment of Yan'an in the Loess Plateau of China (Section 2). Then, we employ multisource remote sensing data, for example, Shuttle Radar Topography Mission (SRTM) Digital Elevation Model (DEM) obtained in 2000, TanDEM-X DEM obtained in 2015, optical Landsat and Copernicus Sentinel-2 images, and two overlapping ascending paths (P11 and P84) of Copernicus Sentinel-1 Synthetic Aperture Radar (SAR) satellite images to monitor the mass transfer, landscape changes, and ground deformation during 2014–2020 (Figure S2). We infer an empirical model to describe the decaying consolidation progress for the regional time-series ground deformation obtained from Interferometric SAR (InSAR) method. Land subsidies while decelerates over the filling areas since the MECC project. The characteristic timescale for land stabilization is about one decade (Section 3). We also apply numerical models to estimate the elastic stress distribution at depth and the attendant three-dimensional (3D) surface elastic displacements and discuss the potential hazards (Section 4).

2. Geological and Geohazard Settings of Yan'an

Yan'an is located at a typical hilly gully region in the central south of the Loess Plateau of China. Loess represents the grayish yellow or brownish yellow and clastic sediments formed by the accumulation of windblown Quaternary aeolian silt. Loess is featured with macro-pores, subvertical joints, loose texture, and high sensitivity to the infiltrated water (Tan, 1964). The first distributary of Yellow River incises into the loess formation in Yan'an. The extensive loess deposits can persist for much of the past 2–3 million years (Pye, 1995) and have a remarkable thickness of hundreds of meters (Figure 1d) (e.g., Liu et al., 1987; Zhuang et al., 2017). The present-day loess structures are a consequence of the loessification processes above the gully bed (Smalley et al., 2006). The loess system is featured with complete stratigraphic sequences with the Late Pleistocene (∼128k–11k year B.P.) Malan Loess at the surface, the underlying Middle Pleistocene (∼730k–128k year B.P.) Lishi Loess, and the Early Pleistocene (∼2.47M–730k year B.P.) Wucheng Loess at the bottom on the paleolandforms (Liu, 1987). Malan Loess is featured with large voids and high structural strength under natural conditions, but it has strong collapsibility or self-weight collapsibility with water. Lishi Loess acts as a good foundation due to its thick calcareous nodules and high density, but it may collapse under high pressure. The new land was created after layered filling and compaction (Li, He, et al., 2018; Qiao et al., 2020). Here the manual filling materials are a mixture of Malan Loess and Lishi Loess. The physical and microstructural properties (e.g., density, porosity, cohesion, friction) of the backfilled loess have changed from the natural condition, resulting in a general weakness of loess skeleton (Ma et al., 2020).

Yan'an has an arid to semi-arid climate, characterized by distinct dry and windy spring, and wet and hot summer. The annual precipitation total is about 450–650 mm. The weak and steep loess slopes are prone to landsliding, which may slip along joints or bedrock. The thick loess may subside when getting wet and disaggregating instantaneously. Loess deformation during Asian monsoonal summer rains may lead to periodic landslide accelerations and sometimes may transition into runout failures (Liu et al., 2020; Meng et al., 2021). About one-third of landslides in China occurred in the Loess Plateau (Juang et al., 2019), in which approximately 15k landslides were detected within the Shaanxi Province (Zhuang et al., 2017). The extreme rainfall in July 2013 triggered widespread lethal landslides in Yan'an that claimed 27 lives. The porous Malan loess contains perpendicular fissures and has high bearing capacity and collapsibility. These physical characteristics result in a high sensitivity to water infiltration. The infiltration depth is usually shallow at a few meters. Increased water content and bulk mass lead to a reduction of shear strength and likely slope failures. Consistently, landslides in Yan'an region are mostly shallow (Wang et al., 2015; Zhuang et al., 2017). The secondary hazards such as river and stream blockages may cause inundation, which may lead to subsequent dam-breaching and engulfing farmlands and villages.

The unprecedented MECC project was reported to start in April 2012 (Li et al., 2014), yet some operations may have initialized locally in the central north and central south of the new land before 2010 as revealed by Landsat-5 image (Figure S1). The MECC project was first performed to the east half of the new land in the first a couple of years. Landsat-7 images illustrate that the land surface was modified in 2012 and then was almost completely flattened over the course of about 1 year in 2013. Thereafter, the MECC project was implemented in the west half of the new land in 2014 when most of the new land had been amended. The landscape modifications were extended further east during 2015–2017. Landsat-7 image in 2017 reveals vegetated areas appeared in the flattened land. The differential NDVI map between 2013 and 2021 derived

from Landsat-8 images demonstrates that the NDVI increased and decreased by similar amount in area (Figures 1 and S3). By the time of the most recent optical image from Sentinel-2 collected in this study (January 3, 2021), the total area of new land amounts to ~20 km^2 (Figure S1).

3. Results

3.1. Topographic Changes

The surface elevation in the newly established urban district north of Yan'an ranges between ~940 and ~1,280 m. The differential map between 2015 TanDEM-X DEM and 2000 SRTM DEM shows pronounced elevation changes by more than ±~80-m difference (Figure S4), agreeing well with the maximum filling thickness (77.6 m) as estimated in the field survey. The surface mass was transported directly from the marginal hilltop areas into the central gullies, rendering a flattened region. The amount of decrease in volume (-1.28×10^8 m^3) is comparable to that of increase (1.27×10^8 m^3). The accuracy of DEM is essential for InSAR processing in areas with drastic landscape alternation and elevation changes like Yan'an. The topographic error of 80 m can yield spurious displacement of 19 mm when applying InSAR method on Sentinel-1 data (see Supplementary Information S1 for details). Therefore, we rely on the most updated free version of 90-m-posting TanDEM-X DEM collected in 2015 in our InSAR analysis.
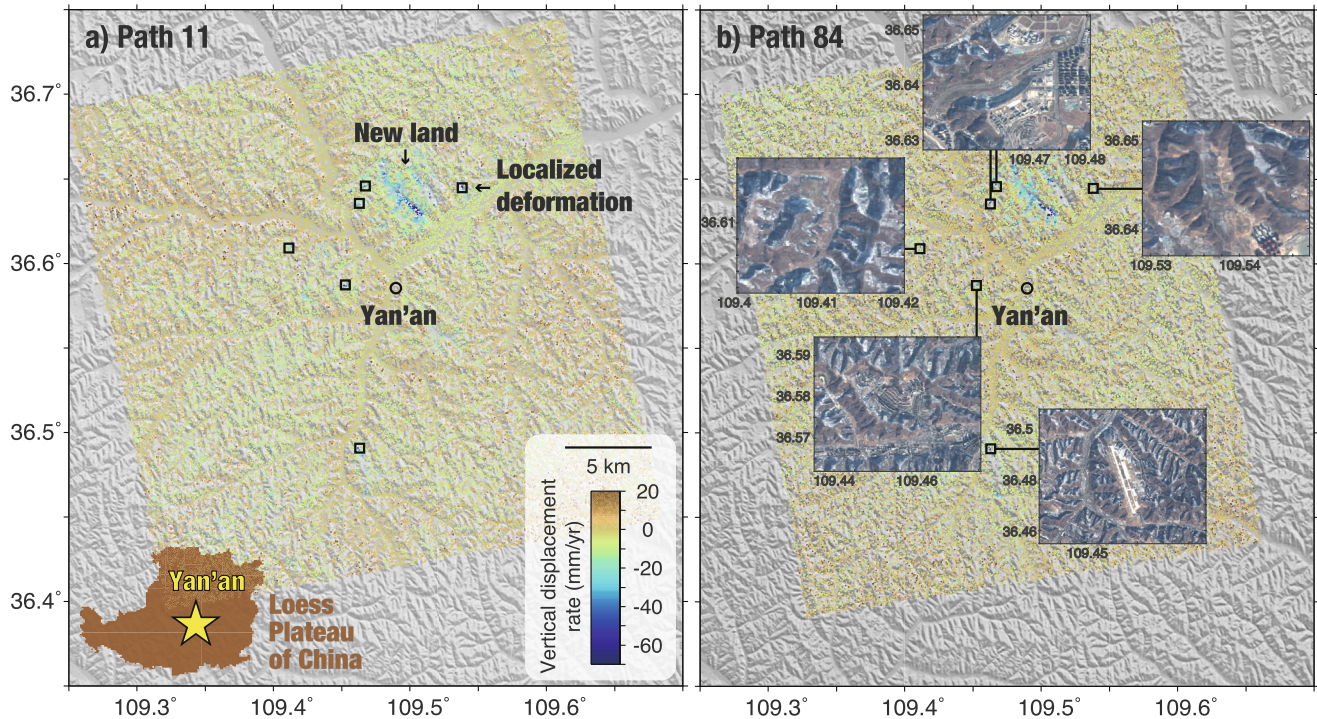
3.2. Spatiotemporal Displacements

Interferograms represent the surface displacements during the repeat-pass acquisitions. Long-wavelength and the elevation-correlated artifacts have been removed from the unwrapped interferograms. Time-series InSAR analysis is in essence the least squares solution of multiple unwrapped interferograms (see Supporting Information S1 for details; Hu et al., 2016). The overlapping Sentinel-1 satellite paths enable us to cross-validate our displacement measurements. Our area of interest is located at the near range and far range of these two paths, respectively, with different incident angles for the projection of displacements from the line-of-sight (LOS) of the SAR satellite to the vertical direction. InSAR results highlight a drastic subsiding area of up to ~70 mm/year to the north of Yan'an downtown where the MECC mega-project has been implemented. The elongated, NW-trending subsiding belt is co-located with previous ditch cuts.

The wetting-induced compaction nature of loess makes the slope vulnerable to slide when saturated such as during the extreme rainfall events in July 2013. We identify six localized unstable slopes/lands where the LOS measurements from both tracks show appreciable subsidence at a rate larger than 40 mm/year (Figure 2). Except for the westernmost one, the other five sites are exposed to anthropogenic alternation and engineering projects and may also experience consolidation settlement.

The data sampling of Path 11 is insufficient before 2016 to resolve the time-series displacements (Figures 3 and S2), so we focus on the recent 3.5 years from late 2016 to early 2020. Results from both paths of 11 and 84 show continuous subsidence though with decreased coherence and signal-to-noise-ratio in the summer monsoon season (Figure 3). No evident seasonal displacement was detected. During the overlapping time frame of these two paths, the displacements measured by Path 11 are consistently slightly larger than those in Path 84, likely due to different imaging geometries and potential horizontal components.

Although the artificial dams prevent widespread silting, there is still considerable mass being trapped in the gullies. The thickest silting mass is 14 m with an average of 7–10 m, covering an area of 2.5×10^5 m^2. These materials are loosely compacted and contain considerable water, which tend to subside upon loading and take long time for stabilization. This represents one of the biggest engineering challenges in the MECC project. The microstructure of loess-like soil governs its creeping behavior (Xie et al., 2018), and the reduced pore microstructure is usually more stable, which renders a practical engineering solution via dynamic compaction, a.k.a., heavy tamping (Zhang, Zhu, et al., 2020). The dynamic compaction is performed in a progressive way, including constructing 4.5-m-depth water drainage ditch. Larger dynamic stresses have been employed for thicker silting mass. For example, the dynamic stresses were set to be 2,000, 3,000, and 6,000 kN·m for silting mass of <5, 5–7, and >7 m, respectively. Plain soils (0.5–1 m thick) and fractured rocks (0.8–1.2 m) are used as the upper and lower cushions, respectively, to support the platform and keep it suitably above the water table. The remolded specimens being compacted have less connected pores than
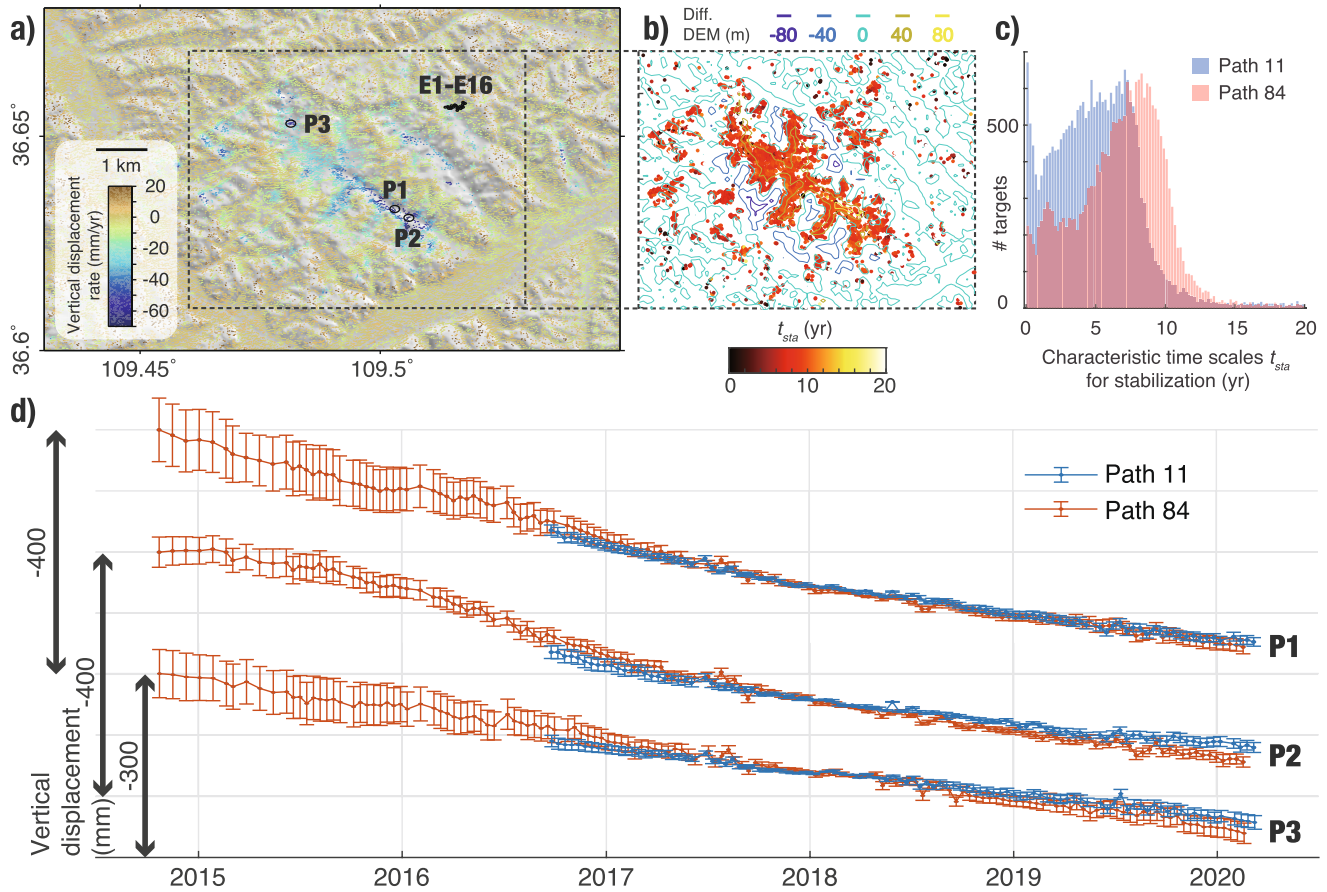
Figure 2. Vertical displacement velocity of Yan'an during 2014–2020. Results from (a) Path 11 and (b) Path 84. Negative values mean subsidence. Six squares represent consistent localized subsiding rates larger than 40 mm/year observed from both two tracks along with their appearance in Sentinel-2 satellite imagery collected on January 3, 2021.

the intact specimens (Zhang, Zhu, et al., 2020), and their soil-water retention conditions are similar (Hou et al., 2020). For targets P1 and P2 in close distance at the center of the fastest subsiding area, their multiannual speed variations differ during 2016 and 2017 (Figure 3), likely due to different operations of dynamic compaction.

3.3. Characteristic Time Scales for Stabilization

To investigate the temporal behavior of the multi-annual deformation, we use an exponential model $a\left(e^{b \cdot t} - 1\right)$ to describe its first-order approximation (Chaussard et al., 2014; Hu et al., 2018; 2020; Shi et al., 2021), where $d(t)$ is the cumulative displacement in meters, t is the cumulative time in years, a characterizes the magnitude of the displacements, and b emphasizes the high orders of derivative (see Supplement Information). The deployment of this model reports a positive magnitude coefficient a and a negative exponent b, suggesting a decreasing time series with decaying rates. The consequent characteristic time scales for stabilization $t_{sta} = \left| \ln\left(\dfrac{\gamma \overline{v}}{ab^2}\right)/b \right|$, where γ is the assumed fraction of the present-day velocity $\overline{v}$. Here the time required for the velocity to diminish to, say, 5% of the present-day rates (e.g., Shi et al., 2021) ranges between 3 and 8.5 years where the extensometers clustered crossing a local depression (Figure S5). The largest rates occur at the longitudinal middle of the gentle slope, agreeing with the behaviors of mass wasting such as landslides.

InSAR results reveal the ground displacements on a regional scale. We first extract targets with comparatively large vertical rates (e.g., < -10 mm/year in this study) and thus sufficiently high signal-to-noise-ratio. Then, we constrain the coefficients a and b using the time series displacements at each target during 2016–2020 for Path 11 and during 2014–2020 for Path 84. We incorporate InSAR-constrained vertical rates $\overline{v}$ to estimate the time scales t_{sta}. Although these two paths have different trajectories and time-series spans, they produce the similar t_{sta} of a couple of decades over the principal filling areas. Therefore, we infer that the

Figure 3. Spatiotemporal vertical displacement of newly established urban area in northern Yan'an. (a) Velocity map and (b) the characteristic time scales for stabilization t_{sta} of targets with large subsidence <-10 mm/year (e.g., from Path 84). Contours in panel b show the differential elevations at 40-m intervals between 2000 SRTM DEM and 2015 Tandem-X DEM. (c) Histograms of t_{sta} from two Sentinel-1 paths. (d) Time-series displacements at three selected targets P1 to P3 (locations shown in panel a). The error bars represent one standard deviation of cumulative displacements measured within 100 m from the target.
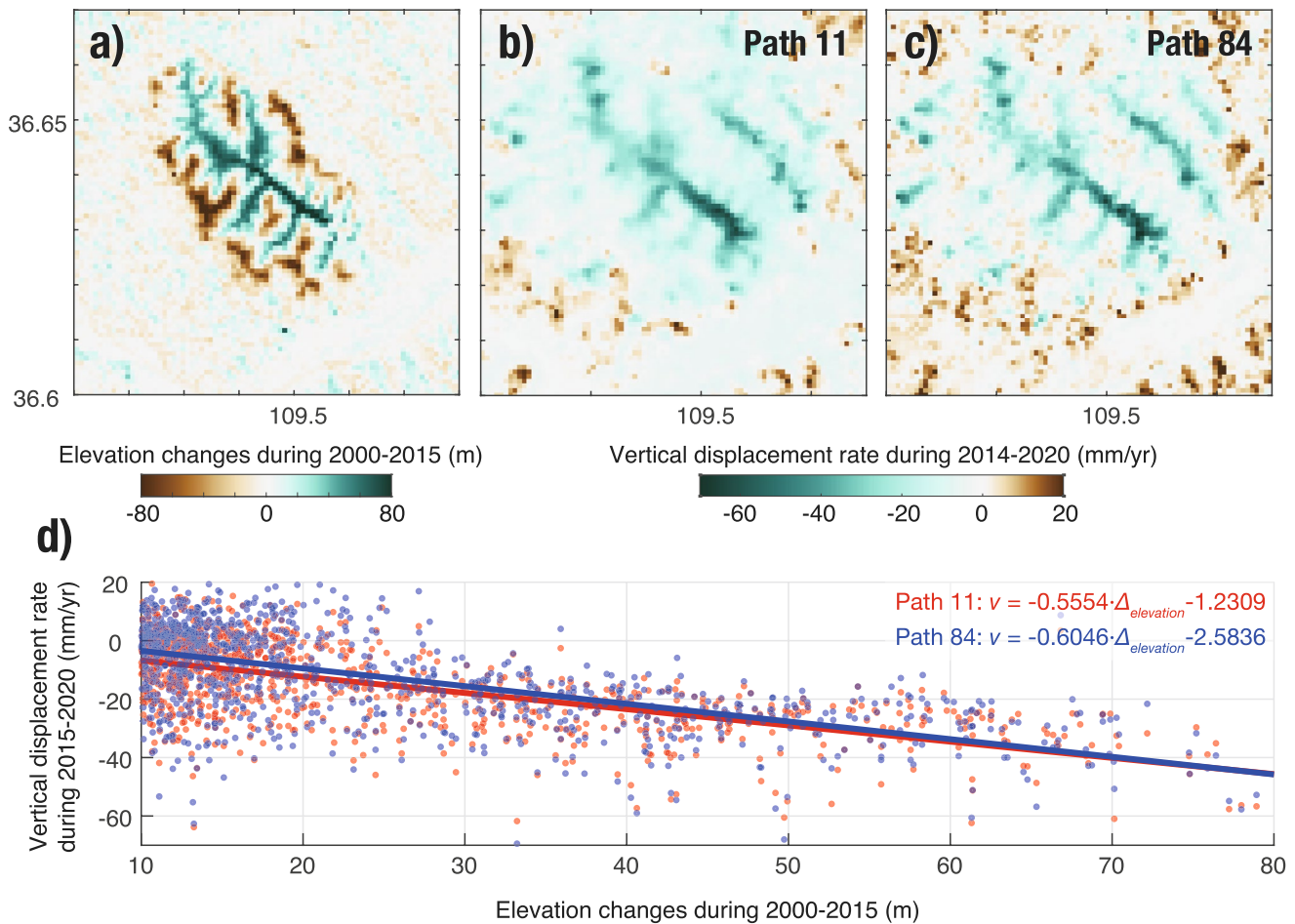
consolidation settlement will be no larger than approximately 3.5 mm/year and reach 5% of the present-day rates, a comparatively stable condition upon 2030 (Figure 3).

4. Discussion

4.1. Correlation Between Landfill and Subsidence

The land subsidence coincides with the surface elevation increase in geographic locations over the new urban area. Intriguingly, the amount of displacement velocity v in mm/year and the 2015–2000 elevation change Δ_{ele} in meters have the first-order correlation. A linear regression reports that $v = -0.56 \times \Delta_{ele} - 1.23$ and $v = -0.60 \times \Delta_{ele} - 2.58$ for the ascending and descending results, respectively (Figure 4). We note that the equations are used to construct the empirical equations relying on the statistics.

For another NW-trending subsiding belt to the east of the major ditch cuts, optical images suggest that this area was still experiencing landfill after the TanDEM-X DEM acquisition in 2015 (Figure S1 and Google Earth), and thus the differential surface elevation map (Figure 4) between 2000 SRTM DEM and 2015 Tan-DEM-X DEM does not appear to have evident changes in this area. Continuous monitoring and updates on the topography are essential for long-term resilience.
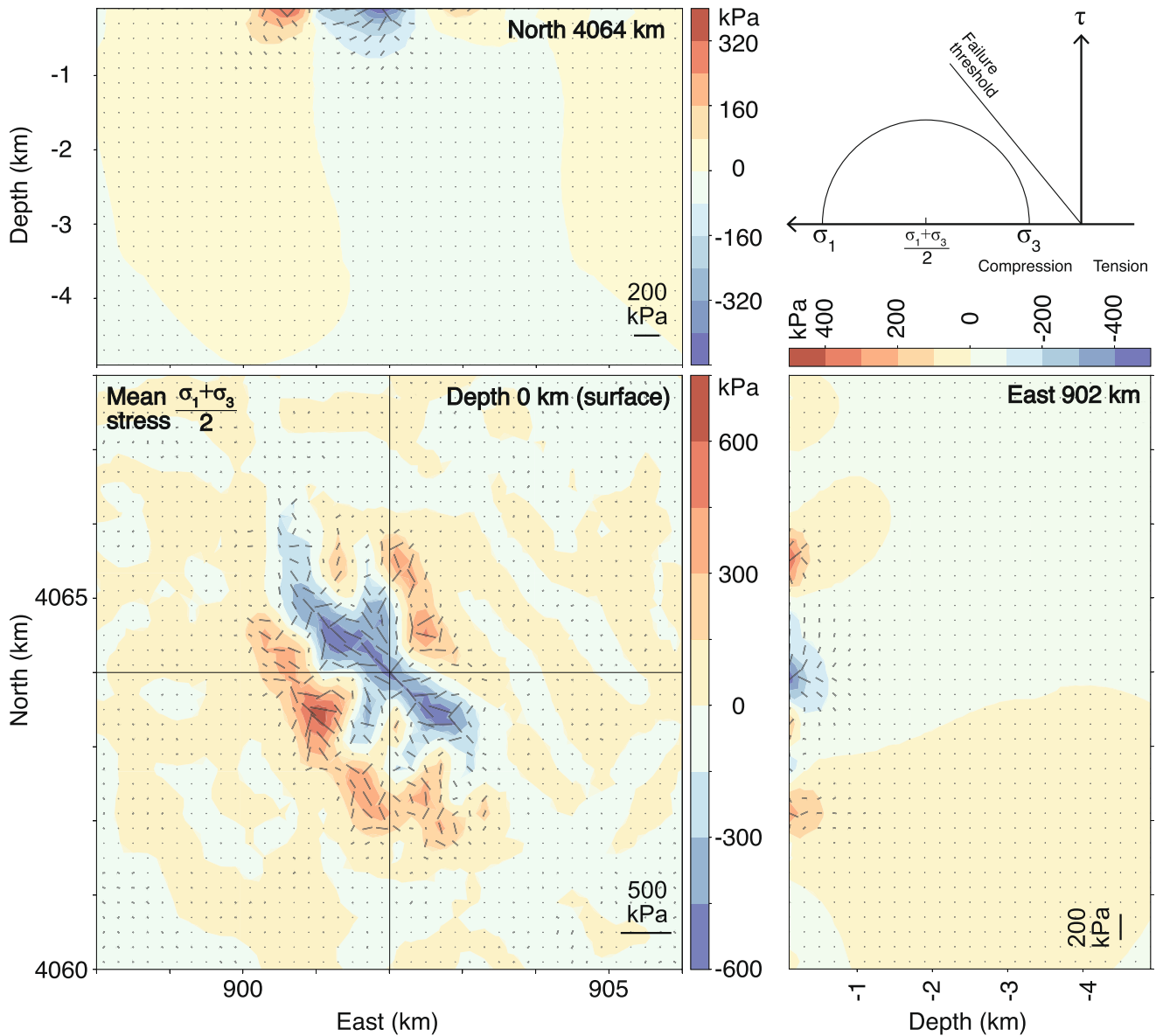
Figure 4. Correlation between the vertical displacements rates v in mm/year and the elevation changes Δ_{ele}. (a) Elevation changes during 2000–2015 from the differential DEM. (b and c) Vertical displacement rate from Path 11 and Path 84, respectively. (d) Linear regression between v and Δ_{ele}, and the root mean square errors are 10.99 and 13.02 for Path 11 and Path 84, respectively.

4.2. Elastic Stress Changes

In addition to ground deformation, the mass transfer can also effectively perturb the shallow elastic stress fields. We consider the Earth structure in the model defined in the global Preliminary Reference Earth Model (PREM), (Dziewonski & Anderson, 1981). The finite element model implemented in PyLith (Aagaard et al., 2013) suggests that the spatial distribution of the principal stress field and the topographic changes are similar. At the ground surface, up to ~600-kPa compressive stress (negative and blue in Figure 5) is concentrated over the elongated gully fills and ~650-kPa tensile stress (positive and red in Figure 5) spreads over the hill cuts at sides. The mean stress $(\sigma_1 + \sigma_3)/2$ peaks at the heart of the individual mass loading and unloading lobes. The horizontal orientations of mean stress (black lines in Figure 5) are aligned with the NW-trending gully fill areas around the central axis and are normal to the stress contours at the marginal stress lobes. Diminishing stresses occur at the intersection between excavations and fills. The mean stress fields diffuse and decay fast with depth and become insignificant from 1-km depth below. For example, the maximum mean stresses reduce to ~100 kPa at 0.5-km depth, ~30 kPa at 1-km depth, ~10 kPa at 2-km depth, and ~5 kPa at 4-km depth.

The forward model helps construct the 3D displacements due to elastic loading/unloading, a different process to the consolidation settlement. The finite element model suggests a maximum of 15 mm elastic deformation due to the surface mass relocation. To be more specific, the filling and loading areas subside by 13 mm while the excavating and unloading areas uplift by 15 mm, and thus the net gradient in vertical

Figure 5. The surface mean stress $(\sigma_1 + \sigma_3)/2$ due to the surface mass relocation in the UTM coordinate system (45 N). Positive in red means tension and negative in blue means compression. The black lines represent the projection of the mean stress on the horizontal panel. Lower left panel shows the stress distribution at the ground surface. Correspondingly, the cross sections along north of 4,064 km and east of 902 km at depth are shown in the upper panel and the lower right panel, respectively. The inset represents the Mohr circle where σ_1 and σ_3 denote the maximum and minimum principal stresses, and the center of the half circle $(\sigma_1 + \sigma_3)/2$ represents the mean stress.

motions reach 28 mm (Figure S6). However, this modeled elastic deformation is instantaneous and insignificant to the cumulative >200 mm surface subsidence as a combination of minor elastic loading and predominant consolidation settlement during 2015–2019. The finite element model of the elastic response of the Earth's crust also gives out a net horizontal shortening and lengthening at distributed locations by up to ~0.6 mm.

Although the formation of the Loess Plateau of China attributes to the tectonic uplift of the Qinghai-Tibet Plateau and the facilitating climatic monsoon, Yan'an is free of active faults and shallow seismogenic structures. However, the vast loess region is subject to appreciable seismic shaking during regional big earthquakes (Zhang & Wang, 2007). On the other hand, the elastic stress perturbations at the shallow crust in the model regime can reach tens to hundreds of kPa. The Mohr-Coulomb circle and the failure envelope

(Figure 5) may intersect and instigate failures when the rainfall-infiltrated pore fluid pressures act effectively in a favorable geometry of the potential critical plane. Moreover, the loess structures make it easier to evolve into loess landslides and loess flow-slides with severe infiltration in Yan'an. For example, more than 8k landslides occurred due to the extremely wet month in July 2013 (Wang et al., 2015), and the Yanlian landslide was triggered by the steam released from heating pipelines of an oil refinery on October 21, 2010 (Hou et al., 2021). Additionally, MECC project includes intensive vegetation removal and reclamation. The differential NDVI map spanning 2013–2021 reveals distributed vegetation changes (NDVI ± 0.5) across the new urban area (Figure 1b). The northern and southern edges show concentrations in the vegetation increase. The linear trace along the roads to the southwest of the new urban area experienced a decrease in vegetation fraction. The damage to the vegetated root systems can reduce the strength of the mass matrix. Therefore, monitoring the slope stability is essential in this naturally landslide-prone region, especially surrounding the excavation sites.

5. Conclusions

Mountain excavation is generally performed for strip mining; however, such mega-scale anthropogenic alternations on the natural environment have never been attempted by mankind for urban expansion. The MECC project in Yan'an is not only an engineering testbed but also a scientific laboratory to investigate if and how human beings would be successful in reshaping the landscape, reforming the Earth's surface process, and reclaiming the heavily modified loess plateau. We synergize multisource satellite remote sensing observations and in-situ geodetic measurements to quantify the surface deformation and subsurface stress due to considerable mass transfer using statistical and finite element models. Differential DEM reveals ±80-m elevation changes and 1.28×10^8-m^3 mass transfer until 2015 when the excavation-filling process had not yet finished. We demonstrate a proportional relationship between the surface subsidence ($<\sim$70 mm/year) and landfill thickness ($<\sim$80 m). We also estimate the characteristic timescale for land stabilization before 2030 using the constrained empirical exponential model. Numerical model of the local mass transfer in elastic half space gives out stress perturbation by hundreds of kilopascals in the shallow crust, which diminishes drastically with depth/distance from the surface loading and unloading source. Our study area is fortunate to be free from active seismogenic structures, yet ground shaking is still possible from big earthquakes around. Overall, our study demonstrates the competence and potentials of remote sensing observations in monitoring and interpreting the surface processes associated with anthropogenic modifications in harsh geological environment. Furthermore, we suggest enacting the reclamation and monitoring to avoid geological and ecological hazards, such as landslides, flood, and pollutions, in this naturally fragile loess environment.

Conflict of Interest

The authors declare no conflicts of interest relevant to this study.

Data Availability Statement

The authors thank the European Space Agency (ESA) for collecting the Copernicus Sentinel-1 SAR data which are available from the Copernicus Open Access Hub (https://scihub.copernicus.eu/dhus/#/home) and the Alaska Satellite Facility (https://search.asf.alaska.edu/), German Space Agency DLR for collecting TanDEM-X DEM (https://download.geoservice.dlr.de/TDM90/), ESA for collecting Copernicus Sentinel-2 optical imagery (https://scihub.copernicus.eu/dhus/#/home), and NASA for collecting Landsat-5/-7 optical imagery (https://landsat.gsfc.nasa.gov/data) and SRTM DEM (https://www2.jpl.nasa.gov/srtm/).

References

Aagaard, B., Kientz, S., Knepley, M., Strand, L., & Williams, C. (2013). *Pylith user manual*. Computational Infrastructure of Geodynamics.

Biggs, J., & Wright, T. J. (2020). How satellite InSAR has grown from opportunistic science to routine monitoring over the last decade. *Nature Communications*, 11, 1-4. https://doi.org/10.1038/s41467-020-17587-6

Burns, S. S. (2007). *Bringing down the mountains: The impact of mountaintop removal surface coal mining on southern West Virginia communities*. West Virginia University Press.

Chaussard, E., Bürgmann, R., Shirzaei, M., Fielding, E., & Baker, B. (2014). Predictability of hydraulic head changes and characterization of aquifer-system and fault properties from InSAR-derived ground deformation. *Journal of Geophysical Research Solid Earth*, *119*(8), 6572–6590. https://doi.org/10.1002/2014jb011266

Chen, F., Guo, H., Ma, P., Lin, H., Wang, C., Ishwaran, N., & Hang, P. (2017). Radar interferometry offers new insights into threats to the Angkor site. *Science Advances*, *3*(3), e1601284. https://doi.org/10.1126/sciadv.1601284

Chen, J., Wu, Y., O'Connor, M., Cardenas, M. B., Schaefer, K., & Kling, G. (2017). Active layer freeze-thaw and water storage dynamics in permafrost environments inferred from InSAR. *Remote Sensing of Environment*, *248*, 112007.

Crotty, M. G. (2002). Bragg v. West Virginia Mining Association: The Eleventh Amendment Challenge to Mountaintop Coal Mining. *Villanova Environmental Law Journal*, *13*, 287.

Dziewonski, A. M., & Anderson, D. L. (1981). Preliminary reference Earth model. *Physics of the Earth and Planetary Interiors*, *25*(4), 297–356. https://doi.org/10.1016/0031-9201(81)90046-7

Fu, B., Wang, S., Liu, Y., Liu, J., Liang, W., & Miao, C. (2017). Hydrogeomorphic ecosystem responses to natural and anthropogenic changes in the Loess Plateau of China. *Annual Review of Earth and Planetary Sciences*, *45*, 223–243. https://doi.org/10.1146/annurev-earth-063016-020552

Handwerger, A. L., Huang, M.-H, Fielding, E. J., Booth, A. M., & Bürgmann, R. (2019). A shift from drought to extreme rainfall drives a stable landslide to catastrophic failure. *Scientific Reports*, *9*(1), 1569. https://doi.org/10.1038/s41598-018-38300-0

He, M. N., Wang, Y. Q., Tong, Y. P., Zhao, Y. L., Qiang, X. K., Song, Y. G., et al. (2020). Evaluation of the environmental effects of intensive land consolidation: A field-based case study of the Chinese Loess Plateau. *Land Use Policy*, *94*, 104523. https://doi.org/10.1016/j.landusepol.2020.104523

Hou, X., Li, T., Qi, S., Guo, S., Li, P., Yi, X., et al. (2021). Investigation of cumulative influence of infiltration on the slope stability with a thick unsaturated zone. *Bulletin of Engineering Geology and the Environment*, *80*, 5467–5480.

Hou, X., Qi, S., Li, T., Guo, S., Yu, W., Li, Y., & Zhang, L. (2020). Microstructure and soil water retention behavior of compacted and intact silt loess. *Engineering Geology*, *277*, 105814.

Hu, X., Bürgmann, R., Schulz, W., & Fielding, E. J. (2020). Four-dimensional surface motions of the Slumgullion landslide and quantification of hydrometeorological forcing. *Nature Communications*, *11*, 2792. https://doi.org/10.1038/s41467-020-16617-7

Hu, X., Lu, Z., & Wang, T. (2018). Characterization of hydrogeological properties in Salt Lake Valley, Utah using InSAR. *Journal of Geophysical Research Earth Surface*, *123*, 1257–1271. https://doi.org/10.1029/2017jf004497

Hu, X., Wang, T., Pierson, T. C., Lu, Z., Kim, J. W., & Cecere, T. H. (2016). Detecting seasonal landslide movement within the Cascade landslide complex (Washington) using time-series SAR imagery. *Remote Sensing of Environment*, *187*, 49–61. https://doi.org/10.1016/j.rse.2016.10.006

Juang, C. H., Dijkstra, T., Wasowski, J., & Meng, X. (2019). Loess geohazards research in China: Advances and challenges for mega engineering projects. *Engineering Geology*, *251*, 1–10. https://doi.org/10.1016/j.enggeo.2019.01.019

Li, P. Y., Qian, H., & Wu, J. H. (2014). Accelerate research on land creation. *Nature*, *510*, 29–31. https://doi.org/10.1038/510029a

Li, Y., He, S., Deng, X., & Xu, Y. (2018). Characterization of macropore structure of Malan loess in NW China based on 3D pipe models constructed by using computed tomography technology. *Journal of Asian Earth Sciences*, *154*, 271–279. https://doi.org/10.1016/j.jseaes.2017.12.028

Li, Z. W., Li, J., Ding, X. L., Wu, L. X., Ke, L. H., Hu, J., et al. (2018). Anomalous glacier changes in the Southeast of Tuomuer-Khan Tengri Mountain Ranges, Central Tianshan. *Journal of Geophysical Research Atmospheres*, *123*, 6840–6863. https://doi.org/10.1029/2017jd028150

Liu, T. S., Zhang, S., & Han, J. M. (1987). Stratigraphy and palaeoenvironmental changes in the loess of central China. *Quaternary Science Reviews*, *6*, 489–501.

Liu, X., Zhao, C., Zhang, Q., Yang, C., & Zhu, W. (2020). Heifangtai loess landslide type and failure mode analysis with ascending and descending Spot-mode TerraSAR-X datasets. *Landslides*, *17*, 205–215. https://doi.org/10.1007/s10346-019-01265-w

Lu, Z., & Dzurisin, D. (2014). *InSAR imaging of Aleutian Volcanoes: Monitoring a volcanic arc from space* (p. 390). Springer Praxis Books, Geophysical Sciences Springer. (ISBN: 978-3-642-00347-9).

Ma, L., Qi, S., Zheng, B., Guo, S., Huang, Q., & Yu X. (2020). Farming influence on physical-mechanical properties and microstructural characteristics of backfilled Loess Farmland in Yan'an, China. *Sustainability*, *12*(14), 5516. https://doi.org/10.3390/su12145516

Meng, Q., Li, W., Raspini, F., Xu, Q., Peng, Y., Ju, Y., et al. (2021). Time-series analysis of the evolution of large-scale loess landslides using InSAR and UAV photogrammetry techniques: A case study in Hongheyan, Gansu Province, Northwest China. *Landslides*, *18*, 251–265. https://doi.org/10.1007/s10346-020-01490-8

Pye, K. (1995). The nature, origin and accumulation of loess. *Quaternary Science Reviews*, *14*(7–8), 653–667. https://doi.org/10.1016/0277-3791(95)00047-x

Qiao, J., Hao, M., & Kong, Y. (2020). Study of deformation characteristics of compacted Q2, Q3 loess in Yan'an region. *Journal of Lanzhou University of Technology*, (In Chinese) *46*(4), 143–149.

Schaefer, L. N., Di Traglia, F., Chaussard, E., Lu, Z., Nolesini, T., & Casagli, N. (2019). Monitoring volcano slope instability with Synthetic Aperture Radar: A review and new data from Pacaya (Guatemala) and Stromboli (Italy) volcanoes. *Earth-Sciences Review*, *192*, 236–257. https://doi.org/10.1016/j.earscirev.2019.03.009

Shi, G. Q., Ma, P., Hu, X., Song, X., Huang, B., & Lin, H. (2021). Surface response and subsurface features during the restriction of groundwater exploitation in Suzhou (China) inferred from decadal SAR interferometry. *Remote Sensing of Environment*, *256*, 112327. https://doi.org/10.1016/j.rse.2021.112327

Shirzaei, M., Freymueller, J., Törnqvist, T. E., Galloway, D. L., Dura, T., & Minderhoud, P. S. J. (2020). Measuring, modelling and projecting coastal land subsidence. *Nature Reviews Earth & Environment*, *2*, 40–58. https://doi.org/10.1038/s43017-020-00115-x

Smalley, I. J., Mavlyanova, N. G., Rakhmatullaev, K. L., Shermatov, M. S., Machalett, B., Dhand, K. O. H., & Jefferson, I. F. (2006). The formation of loess deposits in the Tashkent region and parts of Central Asia; and problems with irrigation, hydrocollapse and soil erosion. *Quaternary International*, *152–153*, 59–69. https://doi.org/10.1016/j.quaint.2005.12.002

Tan, T. K. (1964). Microstructure Classification of Loess in China. *Acta Geologica Sinica*, *44*(3), 357–364.

Wang, G., Li, T., Xing, X., & Zou, Y. (2015). Research on loess flow–slides induced by rainfall in July 2013 in Yan'an, NW China. *Environmental Earth Sciences*, *73*(12), 7933–7944. https://doi.org/10.1007/s12665-014-3951-9

Wang, Z. X. (2017). Boundary data of loess plateau region. *Journal of Global Change Data & Discovery*, *1*(1), 113–114.

Wu, Q., Jia, C., Chen, S., & Li, H. (2019). SBAS-InSAR based deformation detection of urban land, created from mega-scale mountain excavating and valley filling in the Loess Plateau: The case study of Yan'an city. *Remote Sensing*, *11*(14), 1673. https://doi.org/10.3390/rs11141673

Xie, X., Qi, S., Zhao, F., & Wang, D. (2018). Creep behavior and the microstructural evolution of loess-like soil from Xi'an area, China. *Engineering Geology*, *236*, 43–59. https://doi.org/10.1016/j.enggeo.2017.11.003

Xu, Q., Pu, C., Zhao, K., He, P., Zhang, H., & Liu, J. (2021). *Time series InSAR monitoring and analysis of spatio-temporal evolution characteristics of land subsidence in Yan'an new district*. Geomatics and Information Science of Wuhan University. (In Chinese).

Xu, X., Sandwell, D. T., Ward, L. A., Milliner, C. W. D., Smith-Konter, B. R., Fang, P., & Bock, Y. (2020). Surface deformation associated with fractures near the 2019 Ridgecrest earthquake sequence. *Science*, *370*(6516), 605–608. https://doi.org/10.1126/science.abd1690

Zhang, D., & Wang, G. (2007). Study of the 1920 Haiyuan earthquake-induced landslides in loess (China). *Engineering Geology*, *94*(1–2), 76–88. https://doi.org/10.1016/j.enggeo.2007.07.007

Zhang, X., Zhu, W., Li, W., & Zhang, Q. (2020). Monitoring the ground subsidence over Yan'an high-filled region by using time series InSAR technique. *Journal of Engineering Geology*, (In Chinese) *28*(S1), 102–107.

Zhuang, J., Peng, J., Wang, G., Iqbal, J., Wang, Y., Li, W., et al. (2017). Prediction of rainfall-induced shallow landslides in the Loess Plateau, Yan'an, China, using the TRIGRS model. *Earth Surface Processes and Landforms*, *42*, 915–927. https://doi.org/10.1002/esp.4050

References From the Supporting Information

Feng, X., Fu, B., Piao, S., Wang, S., Ciais, P., Zeng, Z., et al. (2016). Revegetation in China's Loess Plateau is approaching sustainable water resource limits. *Nature Climate Change*, *6*, 1019–1022. https://doi.org/10.1038/nclimate3092

Garlanger, J. E. (1972). The consolidation of soils exhibiting creep under constant effective stress. *Géotechnique*, *22*(1), 71–78. https://doi.org/10.1680/geot.1972.22.1.71

Kim, S. W., Wdowinski, S., Dixon, T. H., Amelung, F., Kim, J. W., & Won, J.-S. (2010). Measurements and predictions of subsidence induced by soil consolidation using persistent scatterer InSAR and a hyperbolic model. *Geophysical Research Letters*, *37*, L05304. https://doi.org/10.1029/2009gl041644

Li, X., Li, L., Song, Y., Hong, B., Wang, L., & Sun, J. (2019). Characterization of the mechanisms underlying loess collapsibility for land-creation project in Shaanxi Province, China—A study from a micro perspective. *Engineering Geology*, *249*, 77–88. https://doi.org/10.1016/j.enggeo.2018.12.024

Zhang, L., Qi, S., Ma, L., Guo, S., Li, Z., Li, G., et al. (2020). Three-dimensional pore characterization of intact loess and compacted loess with micron scale computed tomography and mercury intrusion porosimetry. *Scientific Reports*, *10*, 8511. https://doi.org/10.1038/s41598-020-65302-8